Inorganic Chemistry
Cite This: Inorg. Chem. 2018, 57, 1727−1734
Article
pubs.acs.org/IC

Synthesis and Crystal Structure of the Layered Lanthanide Oxychlorides $Ba_3Ln_2O_5Cl_2$

Tiglet Besara,*[,†,‡] Daniel C. Ramirez,[†] Jifeng Sun,[§] Nathaniel W. Falb,[†] Wangwei Lan,[†,∥] Jennifer N. Neu,[†,∥] Jeffrey B. Whalen,[†] David J. Singh,[§] and Theo Siegrist*[,†,⊥]

[†]National High Magnetic Field Laboratory, Florida State University, Tallahassee, Florida 32310, United States
[‡]Department of Physics, Astronomy, and Materials Science, Missouri State University, Springfield, Missouri 65897, United States
[§]Department of Physics and Astronomy, University of Missouri—Columbia, Columbia, Missouri 65211, United States
[∥]Department of Physics, Florida State University, Tallahassee, Florida 32306, United States
[⊥]Department of Chemical and Biomedical Engineering, FAMU−FSU College of Engineering, Florida State University, Tallahassee, Florida 32310, United States

ABSTRACT: Single crystals of a new family of layered lanthanide oxychlorides, $Ba_3Ln_2O_5Cl_2$ (Ln = Gd−Lu), have been synthesized from a molten barium flux. This family crystallizes in the space group $I4/mmm$ (No. 139; $Z = 2$) with lattice parameters $a = 4.3384(1)$−$4.4541(1)$ Å and $c = 24.5108(7)$−$24.8448(9)$ Å. $Ba_3Ln_2O_5Cl_2$ phases are built up of two different blocks: a perovskite double layer of stoichiometry $Ba_2Ln_2O_5$ formed by corner-connected LnO_5 tetragonal bipyramids and a puckered rock-salt-like interlayer of composition $BaCl_2$. A complete structural study along with bond-valence-sum calculations shows that, for lanthanides larger than gadolinium, the structure becomes unstable. Density functional theory calculations show that the valence-band edge is dominated by oxygen orbitals, whereas the conduction band forms from Ba 5d orbitals. The synthesis of this family suggests a route to other potential multianion phases.

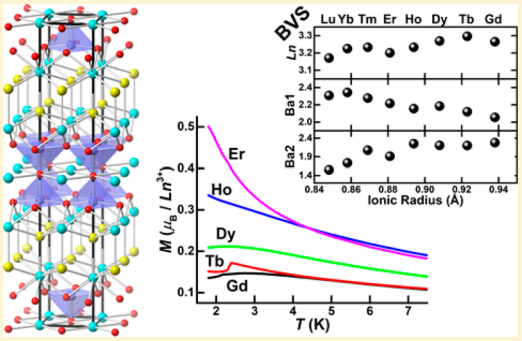

INTRODUCTION

Oxyhalides, with oxygen as well as a halide as anions in a structure, have been extensively studied in the past, such as, e.g., superconductors,[1] frustrated magnets,[2] materials with d-electron delocalization,[3] and photocatalysts.[4] They have also recently shown promise as high-T_C multiferroics.[5] Structurally, the oxygen anion is significantly smaller than the halides, with the exception of the fluorine anion, which is similar in size. The different ionic radii of the halides often produce asymmetric coordination environments around a cation. An example of such a structure type is the BiOCl-type (PbFCl-type), with a planar oxygen square on one side and a planar chlorine square on the other side, with the cation−O bonds at 45° to the cation−Cl bonds. This asymmetric environment produces crystal-field splittings in rare-earth oxyhalide fluorescent materials.[6,7] Other systems, such as the rhombohedral HoOCl in the SmSI-type structure, show a similar asymmetric environment, with four oxygen atoms on one side and three chlorine atoms on the other. Furthermore, semiconducting oxyhalides tend to have smaller band gaps than corresponding oxides because of the lower electronegativities of the halides (with the exception of fluorine) compared to those of oxygen. In many cases, the halide p orbitals are forming the valence-band edge, with the halide p orbitals above the O p orbitals.[8]

Expanding to two different cations with different size and valence is expected to produce an additional separation of the anions because different coordination environments are anticipated for different cations. What remains to be controlled is the reactivity of the two different anions that may lead to multiphase samples. For this, flux methods have proven to be suitable,[9−13] where fluxes with similar solubilities for both oxygen and halides can produce conditions that do not necessarily favor one anion over the other.

Here, we describe the formation of a new barium−lanthanide oxyhalide phase, $Ba_3Ln_2O_5Cl_2$ (Ln = Gd−Lu). This phase contains perovskite bipyramidal $Ba_2Ln_2O_5$ and $BaCl_2$ layers and is structurally related to $Sr_3Fe_2O_5Cl_2$,[14] a $Ba_3Bi_2O_5I_2$-type structure.[15] Other alkaline-earth oxyhalides exist in this structure type, but they all contain either transition metals or other metals, e.g., $Ba_3In_2O_5Cl_2$[16] and $Ba_3Tl_2O_5Cl_2$.[17] To our knowledge, this is the first example of a lanthanide oxyhalide system in this structure type. In addition, magnetic susceptibility measurements of phases containing magnetic lanthanide ions show the onset of magnetic order at low temperature.

Received: September 3, 2017
Published: February 2, 2018

DOI: 10.1021/acs.inorgchem.7b02265
Inorg. Chem. 2018, 57, 1727−1734

Table 1. Lattice Parameters of $Ba_3Ln_2O_5Cl_2$ (Ln = Gd−Lu) Obtained from Single-Crystal X-ray Diffraction Refinement[a]

Ln	M_w (g/mol)	a (Å)	c (Å)	c/a	V (Å^3)	ρ_{calc} (g/cm^3)
Gd	877.42	4.45410(8)	24.8448(9)	5.5780(3)	492.90(3)	5.912
Tb	880.77	4.43171(9)	24.7652(7)	5.5882(2)	486.39(2)	6.014
Dy	887.92	4.40931(9)	24.7407(7)	5.6110(2)	481.01(2)	6.130
Ho	892.78	4.40107(11)	24.6815(9)	5.6081(3)	478.07(3)	6.202
Er	897.44	4.38585(9)	24.6371(9)	5.6174(3)	473.91(3)	6.289
Tm	900.79	4.35954(11)	24.5673(13)	5.6353(4)	466.92(3)	6.407
Yb	909.00	4.33667(12)	24.5745(6)	5.6667(3)	462.17(3)	6.532
Lu	912.86	4.33843(10)	24.5108(7)	5.6497(3)	461.34(3)	6.571

[a]This family of compounds crystallize in the space group $I4/mmm$ (No. 139) with $Z = 2$.

METHODS

Synthesis. Single crystals of $Ba_3Ln_2O_5Cl_2$ (Ln = Gd−Lu) were prepared from a barium metal flux. A total of 1 mmol of Ln_2O_3 powders, 0.25 mmol of BaO powder, and 0.5 mmol of $BaCl_2$ powder were combined with 20 mmol of barium metal pieces. The materials were loaded and sealed in stainless steel crucibles using a TIG welder under an inert (argon) atmosphere in a glovebox. The steel crucibles were then sealed in quartz ampules under vacuum. The samples were heated to 1000 °C in 10 h, solvated for 20 h, and slowly cooled to 820 °C in 200 h. At 820 °C, the ampules were removed from the furnace, inverted, and centrifuged to separate the flux from the crystals. The crystals decomposed in the ambient atmosphere over the course of several hours, first flaking into plates and then decomposing to a powder. To maintain the sample integrity, all crystals were handled and stored under an inert atmosphere. Our flux method simultaneously also produced the secondary phases $BaLn_2O_4$ and LnOCl in single-crystalline form, phases that intergrow with $Ba_3Ln_2O_5Cl_2$.

X-ray Diffraction and Structural Refinement. Single-crystal X-ray diffraction data were collected using an Oxford Diffraction Xcalibur-2 CCD diffractometer with graphite-monochromated Mo Kα radiation. The crystals were mounted in cryoloops under Paratone-N oil and cooled to 200 K with an Oxford Diffraction cryojet. Data were collected using ω scans with 1° frame widths to a resolution of 0.4 Å, equivalent to $2\theta \approx 124°$. Reflections were recorded, indexed, and corrected for absorption using the Rigaku Oxford Diffraction *CrysAlisPro* software,[18] and subsequent calculations were carried out using the X-ray structure refinement and analysis software *CRYSTALS*,[19] employing *Superflip*[20] to solve the crystal structure. The data quality allowed for an unconstrained full-matrix refinement against F^2, with anisotropic thermal displacement parameters for all atoms. CIFs have been deposited with the Cambridge Crystallographic Data Centre (CCDC 1570273−1570280).[21] See Tables 1 and 2 for crystallographic and diffraction details.

Magnetic Measurements. Magnetic susceptibility measurements were carried out using a Quantum Design Magnetic Property Measurements System with an applied field of 1000 Oe in the temperature range 1.8−350 K. All measurements were collected while cooling the samples.

Elemental Analysis. Energy-dispersive spectroscopy using a Zeiss 1540EsB scanning electron microscope equipped with an EDAX Apollo XPP SDD detector was used to confirm the stoichiometry of all compounds, showing a Ba/Ln/O/Cl molar ratio of 3:2:5:2 to within a few percent.

Electronic Structure Calculations. Electronic structure calculations were performed using the linearized augmented plane-wave (LAPW) method,[22] as implemented in the *WIEN2K* code.[23] In the $Ba_3Ln_2O_5Cl_2$ family, we studied $Ba_3Lu_2O_5Cl_2$ because it has a full f shell. The experimental lattice parameters were fixed, but the atomic positions were relaxed with the standard Perdew, Burke, and Ernzerhof functional[24] through total energy minimization. The LAPW sphere radii were 2.4 bohr for barium and lutetium, 2.0 bohr for chlorine, and 1.45 bohr for oxygen. A cutoff parameter $R_{min}K_{max} = 7$ for the basis set was used. A k-point grid of 8 × 8 × 8 was used for the total energy calculations, and a denser k mesh of 17 × 17 × 17 was employed for calculation of the density of states (DOS). An effective Coulomb potential $U = 8$ eV was used for the Lu 4f states. Spin−orbit coupling was included for all of the calculations except structure relaxation.

Table 2. Single-Crystal X-ray Diffraction Refinement Parameters of $Ba_3Ln_2O_5Cl_2$ (Ln = Gd−Lu)[a]

Ln	collected reflns	indep reflns	refined param	R_1	wR_2	GOF on F^2
Gd	10978	1381	18	0.0637	0.0721	0.9998
Tb	10805	1370	18	0.0613	0.0954	1.0000
Dy	10505	1351	18	0.0492	0.0716	0.9996
Ho	10365	1343	18	0.0453	0.0628	0.9986
Er	8392	1324	19	0.0586	0.0858	0.9959
Tm	8256	1295	19	0.0441	0.0665	0.9961
Yb	9968	1298	19	0.0654	0.1124	0.9997
Lu	8175	1298	19	0.0377	0.0464	0.9999

[a]The collection for all crystals was performed at 200 K, and the data collection range for all crystals was $3° \le \theta \le 67°$.

RESULTS AND DISCUSSION

Morphology. The single crystals were transparent, with layered platelike to cubic morphology, although thicker crystals tended to appear opaque. The crystals are expected to be colorless for most of the lanthanides. However, midgap states will produce a reddish color, and the crystals display a range of colors, e.g., purple (Ln = Gd), pink (Ln = Ho), and red (Ln = Lu).

Structure. $Ba_3Ln_2O_5Cl_2$ (Ln = Gd−Lu) crystallizes in the space group $I4/mmm$ (No. 139; $Z = 2$) with lattice parameters $a = 4.3384(1)$−$4.4541(1)$ Å and $c = 24.5108(7)$−$24.8448(9)$ Å for the lutetium analogue to the gadolinium analogue, respectively (see Table 1 for details). The structure of $Ba_3Ln_2O_5Cl_2$ is closely related to the Ruddlesden−Popper-type phase $(ABO_3)_n(AO)$ with $n = 2$, which comprises double layers of ABO_3 perovskites intercalated by single layers of AO rock salt. However, in the case of $Ba_3Ln_2O_5Cl_2$, the perovskite double layers comprise $Ba_2Ln_2O_5$, where one of the apical oxygen positions is replaced by a more distant halide, i.e., bipyramidal defect perovskite blocks of $(BaLnO_{3-x})_2$, and the interlayer, which is a heavily puckered rock-salt-like $BaCl_2$ slab (see Figure 1a).

The Ln^{3+} ions are octahedrally coordinated with five oxygen atoms and one chlorine atom further away, with O2 in the apical position between two lanthanide atoms and the chlorine atom in the opposite apical position. The octahedron is distorted with the lanthanide atom displaced along the c axis, off of the plane formed by the O1 atoms (see Figure 1b). The intercalated slab contains two staggered sheets of BaCl, with both barium and chlorine five-coordinated to the other type.

DOI: 10.1021/acs.inorgchem.7b02265
Inorg. Chem. 2018, 57, 1727−1734

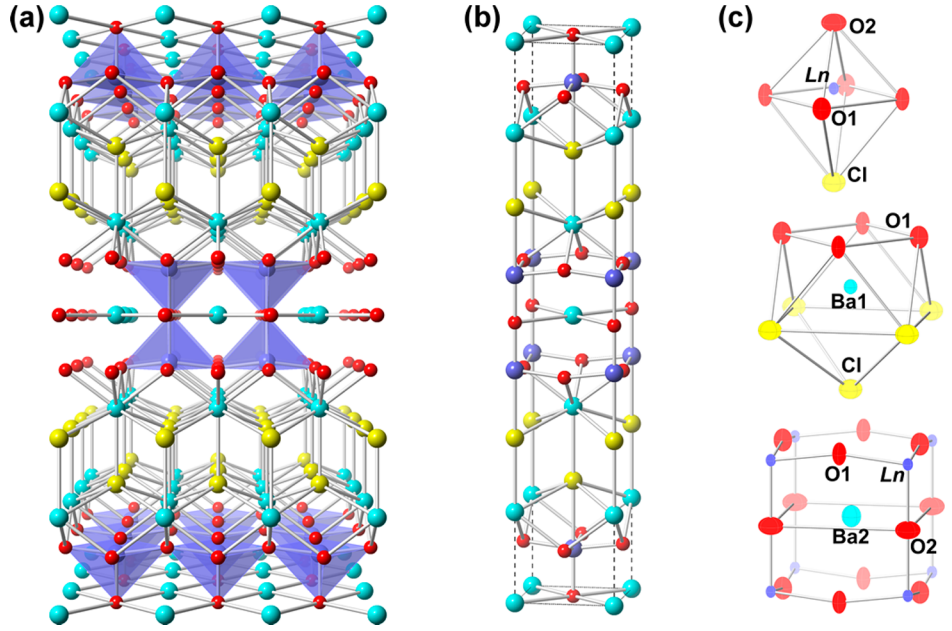

Figure 1. (a) Structure of $Ba_3Ln_2O_5Cl_2$. (b) Unit cell of $Ba_3Ln_2O_5Cl_2$. (c) Atomic environments of Ln, Ba1, and Ba2, displaying anisotropic displacement ellipsoids with 95% probability.

The atomic environment of Ba1 is a 9-fold-coordinated monocapped square-antiprismatic polyhedron with four O1 and five chlorine atoms, while that of Ba2 is a 12-fold-coordinated cuboctahedron of oxygen atoms (eight O1 and four O2 atoms; see Figure 1b), typical for the A position in perovskite ABO_3. The $BaCl_2$ layer separates the perovskite slabs, effectively creating a quasi-two-dimensional system where the intraslab Ln−Ln distances along the *c* axis are approximately 4.16−4.23 Å (via the O2 atom) and 4.34−4.45 Å along the *a* axis (*b* axis; via the O1 atom) for Ln = Lu−Gd, while the interslab distance between the O1-formed equatorial planes (containing lanthanides) in adjacent slabs is approximately 7.57−7.47 Å for Ln = Lu−Gd. Note that the two-dimensional character of the structure is more pronounced as the lanthanide ionic radius shrinks (longer interslab distances and shorter intraslab distances). It should also be noted that the O2 atom between the lanthanide ions on the 4-fold axis shows a large anisotropic displacement parameter due to the short Ln−O2 bond. This will be discussed in more detail below.

$Ba_3Ln_2O_5Cl_2$ is related to the recently discovered compound $Ba_3Yb_2O_5Te$[25] in which the $(BaYbO_{3-x})_2$ double perovskite layers are separated by a CsCl-type slab of BaTe. However, where the perovskite layers were aligned along the *c* axis in $Ba_3Yb_2O_5Te$, the puckered rock-salt-like $BaCl_2$ slab in $Ba_3Ln_2O_5Cl_2$ causes the perovskite layers to stagger, resulting in an approximate doubling of the unit cell along the *c* axis and a change to a body-centered *I*4/*mmm* unit cell. In both $Ba_3Ln_2O_5Cl_2$ and $Ba_3Yb_2O_5Te$, the lanthanide is found on the B site of the ABO_3 perovskite, in contrast to most lanthanide-based ABO_3 perovskites, which find the lanthanide on the A site.

Structural Trends. The unit cell parameters of the $Ba_3Ln_2O_5Cl_2$ series vary systematically with the Ln^{3+} ionic size, as seen in Figure 2, where the parameters are plotted against the ionic radii, as given by Iandelli and Palenzona.[26] As the lanthanide ion progresses from lutetium to gadolinium, the largest absolute effect on the unit cell is along the *c* axis: while *a* changes by 0.116 Å, *c* changes by 0.334 Å. However, the relative

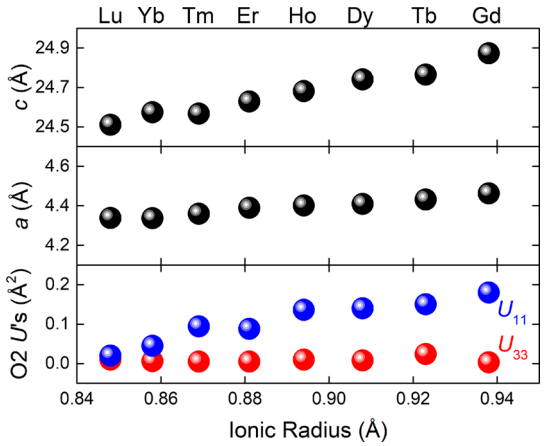

Figure 2. Unit cell parameters *c* (upper panel) and *a* (middle panel) as a function of the ionic radius for $Ba_3Ln_2O_5Cl_2$ (Ln = Gd−Lu). The lower panel displays the anisotropic displacement parameters $U_{11} = U_{22}$ (blue) and U_{33} (red) for the O2 atom located between the lanthanide cations. U_{33} is fairly constant, while $U_{11} = U_{22}$ increases with the ionic radius, indicating a pancake-like probability distribution. Errors bars are within the symbols.

increase is larger along the *a* axis: 2.67% versus 1.36% increase along the *c* axis.

The O2 atom between the lanthanide ions shows a large anisotropic displacement parameter due to the short Ln−O2 bond. The displacement ellipsoids of O2 are pancake-like in their shape, i.e., the large O2 displacement is confined to the *ab* plane, resulting from the squeezed O2 due to the short nominal Ln−O2 bond. The displacement grows and the pancake-like ellipsoid becomes more pronounced as the lanthanide ionic radius increases. As can be seen in the lower panel in Figure 2, the U_{33} anisotropic displacement parameters are fairly constant (and small) as the ionic radius increases, while the $U_{11} = U_{22}$ anisotropic displacement parameters increase linearly with the lanthanide ionic radius (from 0.02 $Å^2$ for $Ba_3Lu_2O_5Cl_2$ to 0.18 $Å^2$ for $Ba_3Gd_2O_5Cl_2$), becoming a pronouncedly more oblate

DOI: 10.1021/acs.inorgchem.7b02265
Inorg. Chem. 2018, 57, 1727−1734

anisotropic displacement ellipsoid as the series progresses from the lutetium phase to the gadolinium phase. Splitting the O2 atom into four positions away from the ideal position did not improve the overall fit to the data, and, therefore, the ideal position was retained for the CIF. However, a displacement away from the ideal position increases the Ln−O2 distance while decreasing/increasing the Ba2−O2 distance. Furthermore, no superstructure reflections were observed, indicating the random disorder of O2.

As mentioned before, the lanthanide octahedron is distorted, with the lanthanide ion displaced along the *c* axis toward the apical oxygen O2, to a position slightly inside the tetragonal bipyramid formed by the oxygen atoms. As the $Ba_3Ln_2O_5Cl_2$ series progresses from lutetium to gadolinium, this distortion increases, i.e., the angle O1−Ln−O1 along the *a* or *b* axis shifts further away from 180° for an "ideal" octahedron, where the center atom is in the plane formed by the equatorial atoms. This can be seen in the lower panel of Figure 3: the angle

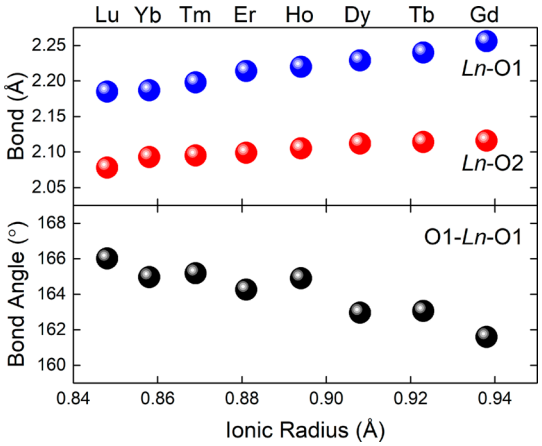

Figure 3. Top: Bond lengths of Ln to O1 and O2. Bottom: Angle O1−Ln−O1 along the *a* or *b* axis. Errors bars are within the symbols.

decreases from approximately 166.0° for $Ba_3Lu_2O_5Cl_2$ to approximately 161.6° for $Ba_3Gd_2O_5Cl_2$. As expected, the bond lengths increase as the lanthanide ions increase in size (upper panel of Figure 3), the equatorial Ln−O1 bond more so than the apical Ln−O2 bond.

The question naturally arises, why could none of the remaining compounds in this family be successfully synthesized, viz., $Ba_3Ln_2O_5Cl_2$ (Ln = La−Eu)? In fact, we have shown previously that a whole series of barium lanthanide oxides, the $BaLn_2O_4$ (Ln = La−Lu) family, can be successfully synthesized in single-crystalline form.[27] In order to shed light on this, we evaluated the bond valence sum (BVS) for the different cations. The results of the BVS calculations are shown in Figure 4, as a function of the lanthanide ionic radii. Calculating these BVSs, we used the extrapolated values, as given by Brese and O'Keeffe,[28] for the Ln−O, Ln−Cl, and Ba−Cl bonds and the newly derived values by Gagné and Hawthorne[29] for the Ba−O bonds. As discussed above, the large anisotropic displacement parameter of the O2 atom that increases progressively as the series progresses from the lutetium phase to the gadolinium phase (see the lower panel in Figure 2) suggests that O2 is randomly displaced from its ideal position. Therefore, upon calculation of the BVS for lanthanide and Ba2 (O2 does not affect the BVS for Ba1), two situations were considered: one where the ideal position of O2 was retained and one where the

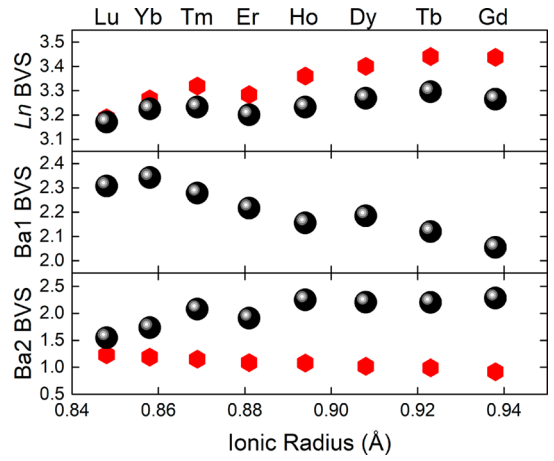

Figure 4. BVSs for the lanthanide (upper panel), Ba1 (middle panel), and Ba2 (lower panel) cations. The small red hexagons are the BVSs using the ideal positions of the O2 atoms, while the large black spheres are the BVSs taking into account the anisotropic displacement of O2 (the Ba1 BVS is not affected by O2). Errors bars are within the symbols.

random displacement was taken into account, resulting in longer Ln−O2 distances and shorter Ba2−O2 distances. The upper panel in Figure 4 shows the BVS of the lanthanide ions, and already a trend toward instability for larger cations becomes apparent. Using the ideal position of O2 (shown as red hexagons), the BVS is consistently above the expected valence of 3 with BVS ≈ 3.2 for the lutetium phase and approaching BVS ≈ 3.5 for the gadolinium phase. The BVS is much reduced when taking into account the O2 displacement (shown as black spheres) but also show values in excess of 3. This overbonding (high BVS) of the lanthanide cations can be attributed to the short bond to the apical O2, which is squeezed between two lanthanide ions. This bond length increases as the series progresses from the lutetium phase to the gadolinium phase (see Figure 3), but that increase is explained by the lanthanide ion size. The Ba1 cations are part of the intercalated $BaCl_2$ slab and trend toward the expected BVS of 2 (middle panel in Figure 4) with increasing lanthanide ion size. In contrast, the BVS of the Ba2 cations shows a different trend (lower panel in Figure 4): the Ba2 cations are part of the double perovskite layers and in-plane with the heavily squeezed O2. Despite an environment of 12 oxygen atoms (see Figure 1b), the Ba2 cation is strongly underbonded (low BVS) with a BVS ≈ 1.2 for the lutetium phase and reaching BVS ≈ 0.9 for the gadolinium phase, when considering the ideal position of the O2 atom (red hexagons). This indicates that the cavity formed by the 12 oxygen atoms is too large for the barium cation. However, taking into account the O2 displacement, the picture changes. The Ba2 BVS including the displacement (black spheres) increases instead of decreasing with the ionic radius: from underbonded 1.5 for the lutetium phase to overbonded 2.4 for the gadolinium phase. It is clear that the O2 displacement (reflected in the oblate displacement ellipsoid) has to be taken into account to provide a better picture of the local Ba2 bonding conditions. With the lanthanide cations overbonded and the Ba2 cations ranging from underbonding to overbonding, these two cations in the double perovskite layer compensate for each other and stabilize the highly strained structure where lattice expansion and contraction balance. However, this stabilization seems to only go as far as the

DOI: 10.1021/acs.inorgchem.7b02265
Inorg. Chem. 2018, 57, 1727−1734

gadolinium compound, and for lanthanide ions larger than gadolinium, the structure is expected to become unstable because the BVSs of lanthanide and Ba2 both increase the overbonding levels. Therefore, a stability limit on this family of compounds can be placed close to the gadolinium radius.

Magnetization. Figure 5 displays the low-temperature region of magnetization $M(T)$ for the Ln = Gd−Er members of

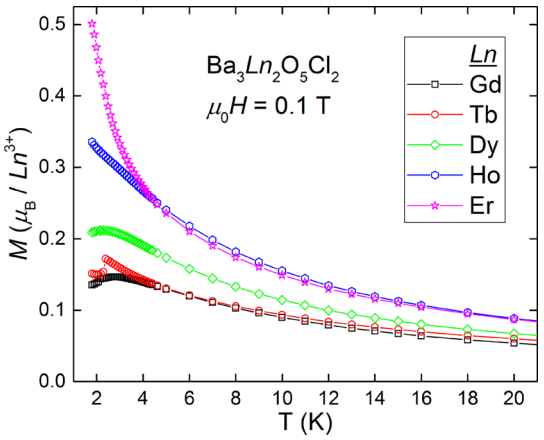

Figure 5. Magnetization as a function of temperature, measured at an applied field of 0.1 T for $Ba_3Ln_2O_5Cl_2$ (Ln = Gd−Er).

$Ba_3Ln_2O_5Cl_2$. The lutetium phase is nonmagnetic, and for Ln = Tm and Yb, not enough pristine $Ba_3Ln_2O_5Cl_2$ sample mass could be extracted to perform reliable magnetization measurements because the crystals were embedded in the secondary phases $BaLn_2O_4$ and LnOCl, both providing a magnetic signal of similar magnitude. $Ba_3Gd_2O_5Cl_2$ and $Ba_3Dy_2O_5Cl_2$ display a broad maximum at approximately 2.8 and 2.3 K, respectively, indicating an onset of antiferromagnetic order at lower temperatures. $Ba_3Tb_2O_5Cl_2$, on the other hand, exhibits a sharp transition to long-range antiferromagnetic ordering at approximately 2.5 K. In contrast, $Ba_3Ho_2O_5Cl_2$ and $Ba_3Er_2O_5Cl_2$ seemingly display Curie−Weiss paramagnetism down to the lowest temperatures, with $Ba_3Er_2O_5Cl_2$ having a steeper increase in $M(T)$ at low temperatures.

However, this picture needs to be modified. Looking at the derivatives of the magnetization (Figure 6), the erbium phase exhibits an inversion of dM/dT at about 2 K, indicating a reduction of the steep increase. Estimating a transition temperature using this inversion by extrapolating dM/dT to zero yields a transition temperature of approximately 0.95 K for $Ba_3Er_2O_5Cl_2$. The holmium phase, on the other hand, never exhibits a turn in dM/dT in the temperature range measured but instead exhibits a plateau at approximately 2−4 K, before rapidly dropping again. It is not clear as to what the nature of this plateau in dM/dT is; however, the plateau may be the start of an inversion in dM/dT, as seen in the other compounds, but because of magnetic impurities giving a Curie tail, the magnetization increases further, resulting in a rapid drop in dM/dT (increase in magnetization with decreasing temperature). Such an increase in magnetization at the very lowest temperatures can also be seen in the terbium phase.

All compounds display Curie−Weiss behavior at high temperatures (Figure 6). Because of the limitation of obtaining a sufficient mass of pristine samples (the samples included flux residue along with secondary phases), the measured effective moments deviate from the expected free ion values derived at

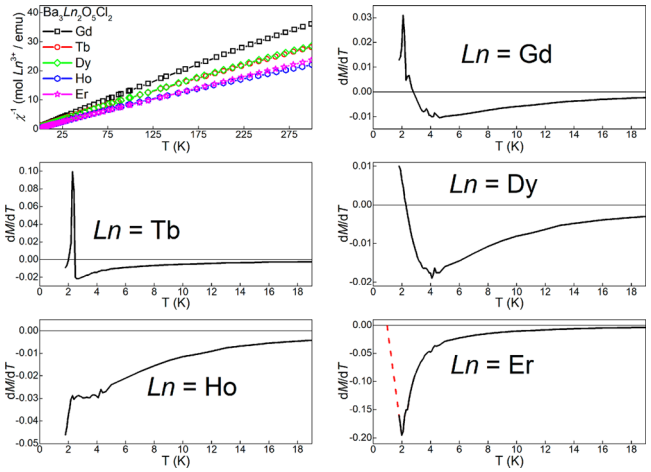

Figure 6. Top left panel: Inverse susceptibility as a function of the temperature for $Ba_3Ln_2O_5Cl_2$ (Ln = Gd−Er). All compounds display Curie−Weiss behavior at high temperatures. All other panels: Derivatives of the magnetization, dM/dT, at low temperatures, with $dM/dT = 0$ marked by a horizontal line. The red dashed line in the erbium phase figure is an extrapolation.

high temperatures (200−300 K; see Table 3). The Weiss temperatures are all negative, indicating antiferromagnetic

Table 3. Effective Magnetic Moments and Weiss Temperatures for $Ba_3Ln_2O_5Cl_2$ (Ln = Gd−Er), Obtained from the High-Temperature Curie−Weiss Fits of $\chi^{-1}(T)$[a]

Ln^{3+}	m (mg)	μ_{calcd} (μ_B)	μ_{eff} (μ_B)	θ_W (K)	f
Gd^{3+}	29.5	7.94	8.54(3)	−29(2)	10(1)
Tb^{3+}	16.8	9.72	9.65(2)	−29(1)	12(1)
Dy^{3+}	21.1	10.65	9.65(2)	−33(2)	14(1)
Ho^{3+}	43.5	10.61	11.08(3)	−39(2)	
Er^{3+}	20.8	9.58	10.20(1)	−8(1)	8.5[b]

[a]The last column is the frustration index. [b]Obtained by the extrapolation of dM/dT to zero.

interactions between lanthanide ions, and hint at Néel temperatures about 10 times larger than those observed. It should be noted that $Ba_3Er_2O_5Cl_2$ has a distinctly lower Weiss temperature than the other members, which may be attributed to crystal-field splitting of the Er 4f energy levels.

The suppressed ordering temperature is a manifestation of crystal-field effects and possibly frustration, likely induced by the disordered O2 atoms. Using the temperature values when $dM/dT = 0$ as the transition temperatures, a frustration index[30] $f = |\theta_W|/T_N$ is obtained for these compounds except for $Ba_3Ho_2O_5Cl_2$, which never reaches $dM/dT = 0$. In the case of $Ba_3Gd_2O_5Cl_2$ and $Ba_3Dy_2O_5Cl_2$, the broad maxima are taken as the transition temperatures, and in the case of $Ba_3Er_2O_5Cl_2$, the extrapolation of dM/dT to zero gives the transition temperature. The frustration index is on the order of ∼10 for all of the compounds studied, with $Ba_3Dy_2O_5Cl_2$ exhibiting the highest frustration. Following the arguments by Ramirez,[30] these compounds can be considered to be moderately to strongly frustrated materials.

As was already discussed in the Structure section, the $Ba_3Ln_2O_5Cl_2$ structure is a quasi-two-dimensional system, with interslab distances approximately 68−74% longer than intraslab Ln−Ln distances, and the two-dimensional character becomes more pronounced with decreasing lanthanide ionic radius. The

DOI: 10.1021/acs.inorgchem.7b02265
Inorg. Chem. 2018, 57, 1727−1734

magnetization and magnetic structures of the isostructural transition-metal compounds $Sr_3(Fe,Co)_2O_5Cl_2$ and $Sr_3FeCoO_5Cl_2$ have been studied by neutron diffraction,[31] where it was shown that they adopt a G-type antiferromagnetic structure[32] (i.e., both intraplane and interplane magnetic interactions are antiferromagnetic) and that the magnetic moments are confined to the *xy* plane. The $Ba_3Ln_2O_5Cl_2$ compounds all have a negative Weiss constant (see Table 3) and, therefore, also exhibit antiferromagnetism. Within the scope of the current study, it cannot be discerned which type of antiferromagnetism is present in the $Ba_3Ln_2O_5Cl_2$ compounds. The different low-temperature behavior (Figure 5) may be due to the different magnetic configurations, which depend on the crystal-field effects, anisotropy, and ground-state configurations. In fact, a theoretical study on the superexchange interactions between lanthanide ions showed that, in the case of f^1−f^1 superexchange, the anisotropy is due to a combination of spin−orbit coupling, crystal-field effects, intraionic interactions, and anisotropic overlaps between the Ln 4f and 5d orbitals and the *n*p orbitals of the bridging ligands.[33] The difference between the sharp transition of $Ba_3Tb_2O_5Cl_2$ and the broad maxima of $Ba_3Gd_2O_5Cl_2$ and $Ba_3Dy_2O_5Cl_2$ may be due to a different antiferromagnetic type, resulting from the anisotropy. A neutron diffraction study, beyond the scope of this work, should elucidate this.

Electronic Structure Calculations. Figure 7 displays the results of the orbital projected density of states (PDOS, upper panel) and total density of states (TDOS, lower panel) for nonmagnetic $Ba_3Lu_2O_5Cl_2$, as obtained from an electronic structure calculation. This phase was chosen because the 4f levels are located well below the Fermi level, and the displacement of O2 from the ideal position is small enough to be neglected. Indeed, the full f^{14} Lu 4f states reside deep in the valence band and are seen as sharp peaks between −4 and −6 eV (seen in the TDOS), emphasizing the localized character of the f-shell electrons. The deeper states between −9 and −13 eV are the Ba 5p states. The two sites of O 2p and Cl 3p states dominate the valence band close to the Fermi energy, with the O1 2p states, which make up the equatorial base of the lanthanide-centered octahedra, forming the valence-band edge despite oxygen being more electronegative than chlorine. This is in contrast to $Ba_3Yb_2O_5Te$,[25] where the valence-band edge is formed by the much less electronegative Te 5p states. The conduction band is dominated by the empty Ba 5d states, with contributions from the Lu 5d and O1 2p states (see the inset in the lower panel of Figure 7). The band gap of approximately 3.72 eV is thus formed by the O1 2p and Ba1 and Ba2 5d states.

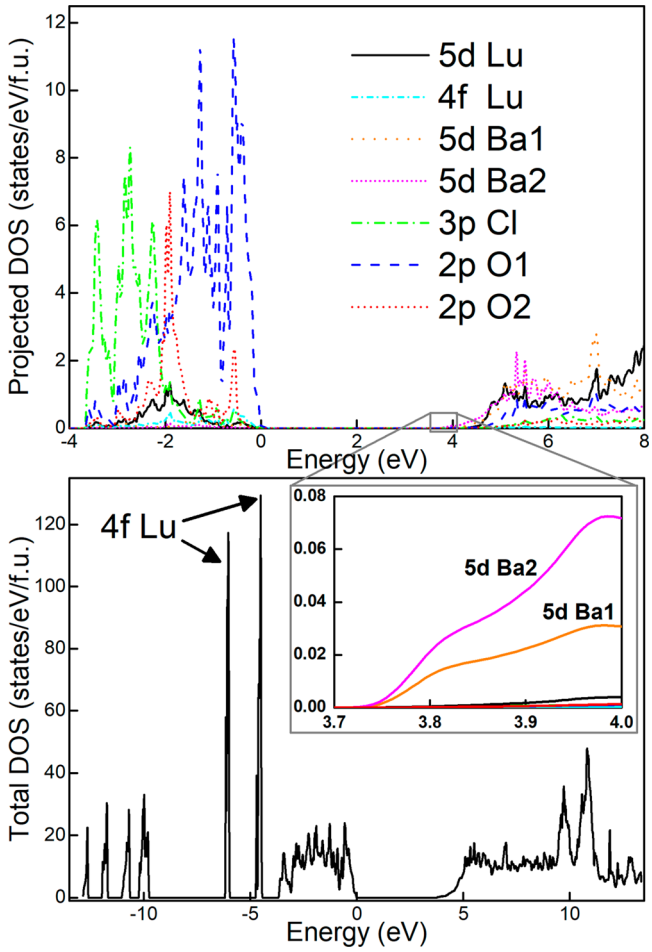

Figure 7. Top: Orbital PDOS for $Ba_3Lu_2O_5Cl_2$. Bottom: TDOS. The inset in the lower panel is a close-up view of the conduction-band edge, showing that it is dominated by the empty Ba 5d states.

CONCLUSION

The multianion phases of $Ba_3Ln_2O_5Cl_2$ combine two distinct structural units, $Ba_2Ln_2O_5$ bipyramidal perovskite-type layers with the barium atoms on the perovskite A sites and lanthanide atoms on the perovskite B- sites. This unit is quite stable for the second half of the lanthanide series, from gadolinium to lutetium. However, the structure does not form via ceramic methods of combining powders of BaO, Ln_2O_3, and $BaCl_2$ and heating at elevated temperatures. No further efforts were undertaken to optimize the phase formation for ceramic techniques. The presence of a large lanthanide ion on the perovskite B site clearly strains the lattice, reflected in the overbonding observed in the BVS for the lanthanides and Ba2. Attempts to synthesize the samarium phase did not give reproducible results, and no phase formation was observed for neodymium and lanthanum. It is, furthermore, clearly shown in the BVS calculations that trivalent atoms smaller than lutetium (such as scandium) may increase the phase stability. While not many perovskite-type phases are known where the lanthanide occupies the perovskite B site, the bipyramidal perovskite layer is stable for a number of smaller lanthanides and has also been observed in $Ba_3Yb_2O_5Te$.[25] However, $Ba_3Yb_2O_5Te$ has no analogues with lanthanides larger than ytterbium.

The $BaCl_2$ layer separating the bipyramidal perovskite layer $Ba_2Ln_2O_5$ is structurally better matched to the different lanthanide sizes and helps to stabilize the highly strained $Ba_2Ln_2O_5$ layers for larger-radii lanthanides, up to gadolinium. Further changes of the separation layer, for instance, using $BaBr_2$ or BaClBr, could conceivably extend the stability range of the $Ba_2Ln_2O_5$ layers to larger lanthanides. However, the short Ln−O distances and disorder are likely to affect the overall stability.

The magnetic susceptibility data indicate potential low-temperature magnetic order and, for some of the elements, fairly strong crystal-field splitting. For the gadolinium atom, however, no crystal-field effects are expected for the $S_{7/2}$ state. Indeed, the magnetic susceptibility follows a Curie−Weiss law, with a small Weiss constant, and the onset of antiferromagnetic order at around 2.7 K. This order onset is likely two-dimensional, with three-dimensional order expected at lower temperatures. This is due to the anisotropic crystal structure,

DOI: 10.1021/acs.inorgchem.7b02265
Inorg. Chem. 2018, 57, 1727−1734

where interlayer interactions require extended superexchange paths via the $BaCl_2$ layers.

A potentially homologous series of $mBa_2Ln_2O_5 + nBaCl_2$ with $n \geq m$ may exist, but so far, no indication of such phases was observed. Furthermore, other combinations producing new multianion systems may ultimately be possible, such as, for instance, $2Ba_2Ln_2O_5 + BaCl_2 + BaTe = Ba_6Ln_4O_{10}Cl_2Te$. For single-crystal growth of such systems, the flux described in this work may be suitable because concurrent solubility for oxygen and tellurium and also oxygen and chlorine in molten barium is demonstrated.

In conclusion, we have achieved crystal growth of a complex multianion system, $Ba_3Ln_2O_5Cl_2$, using molten alkaline-earth metals as a flux. The crystal structure suggests a potential homologous series, as well as other potential multianion phases, with a route to obtaining single crystals via growth from alkaline-earth fluxes.

■ ASSOCIATED CONTENT

Accession Codes

CCDC 1570273−1570280 contain the supplementary crystallographic data for this paper. These data can be obtained free of charge via www.ccdc.cam.ac.uk/data_request/cif, or by emailing data_request@ccdc.cam.ac.uk, or by contacting The Cambridge Crystallographic Data Centre, 12 Union Road, Cambridge CB2 1EZ, UK; fax: +44 1223 336033.

■ AUTHOR INFORMATION

Corresponding Authors

*E-mail: tigletbesara@missouristate.edu.
*E-mail: siegrist@magnet.fsu.edu.

ORCID

Tiglet Besara: 0000-0002-2143-2254

Notes

The authors declare no competing financial interest.

■ ACKNOWLEDGMENTS

A portion of this work was performed at the National High Magnetic Field Laboratory, which is supported by National Science Foundation Cooperative Agreement DMR-1157490 and the State of Florida. T.B., D.C.R., and T.S. acknowledge support from the U.S. Department of Energy, Office of Basic Energy Sciences, Division of Materials Sciences, under Award DE-SC0008832. Work at the University of Missouri was supported by the Department of Energy through the S3TEC Energy Frontier Research Center, Award DE-SC0001299.

■ REFERENCES

(1) Adachi, S.; Tatsuki, T.; Tamura, T.; Tanabe, K. Halooxocuprate Superconductors and Related Compounds with the $02(n\text{-}1)n$ and 0222 Structures. *Chem. Mater.* **1998**, *10*, 2860−2869.

(2) Tsirlin, A. A.; Rosner, H. Structural Distortion and Frustrated Magnetic Interactions in the Layered Copper Oxychloride (CuCl)-$LaNb_2O_7$. *Phys. Rev. B: Condens. Matter Mater. Phys.* **2009**, *79*, 214416.

(3) Wilson, J. A.; Maule, C.; Strange, P.; Tothill, J. N. Anomalous Behaviour in the Layer Halides and Oxyhalides of Titanium and Vanadium: A Study of Materials close to Delocalisation. *J. Phys. C: Solid State Phys.* **1987**, *20*, 4159−4167.

(4) Li, J.; Yu, Y.; Zhang, L. Bismuth Oxyhalide Nanomaterials: Layered Structures Meet Photocatalysis. *Nanoscale* **2014**, *6*, 8473−8488.

(5) Zhao, L.; Fernández-Díaz, M. T.; Tjeng, L. H.; Komarek, A. C. Oxyhalides: A New Class of High-T_C Multiferroic Materials. *Sci. Adv.* **2016**, *2*, e1600353.

(6) Kim, D.; Park, S.; Kim, S.; Kang, S.-G.; Park, J.-C. Blue-Emitting Eu^{2+}-Activated LaOX (X = Cl, Br, and I) Materials: Crystal Field Effect. *Inorg. Chem.* **2014**, *53* (22), 11966−11973.

(7) Wang, Q.; Gao, Y.; Bulou, A. Crystal Field and Free-Ion Analysis for Eu^{3+} Ion in LaOF Crystal. *J. Phys. Chem. Solids* **1995**, *56* (2), 285−291.

(8) Kaminskii, A. A. *Laser Crystals. Their Physics and Properties*, 2nd ed.; Springer Series in Optical Sciences; Springer-Verlag: Berlin, 1990.

(9) Ackerman, J. F. The Preparation and Structures of the Alkaline Earth Iron Oxyhalides. *J. Solid State Chem.* **1991**, *92*, 496−513.

(10) Read, C. M.; Yeon, J.; Smith, M. D.; zur Loye, H.-C. Crystal Growth, Structural Characterization, Cation-Cation Interaction Classification, and Optical Properties of uranium(VI) Containing Oxychlorides, $A_4U_5O_{16}Cl_2$ (A = K, Rb), $Cs_5U_7O_{22}Cl_3$, and AUO_3Cl (A = Rb, Cs). *CrystEngComm* **2014**, *16*, 7259−7267.

(11) Latshaw, A. M.; Hughey, K. D.; Smith, M. D.; Yeon, J.; zur Loye, H.-C. Photoluminescent and Magnetic Properties of Lanthanide Containing Apatites: $Na_xLn_{10-x}(SiO_4)_6O_{2-y}F_y$, $Ca_xLn_{10-x}(SiO_4)_6O_{2-y}F_y$ (Ln = Eu, Gd, and Sm), $Gd_{9.34}(SiO_4)_6O_2$, and $K_{1.32}Pr_{8.68}(SiO_4)_6O_{1.36}F_{0.64}$. *Inorg. Chem.* **2015**, *54*, 876−884.

(12) Morrison, G.; Smith, M. D.; zur Loye, H.-C. Understanding the Formation of Salt-Inclusion Phases: An Enhanced Flux Growth Method for the Targeted Synthesis of Salt-Inclusion Cesium Halide Uranyl Silicates. *J. Am. Chem. Soc.* **2016**, *138*, 7121−7129.

(13) Abeysinghe, D.; Smith, M. D.; zur Loye, H.-C. A Fresnoite-Structure-Related Mixed Valent titanium(III/IV) Chlorosilicate, $Ba_3Ti_2Si_4O_{14}Cl$: A Flux Crystal Growth Route to Ti(III) Containing Oxides. *J. Solid State Chem.* **2017**, *250*, 128−133.

(14) Leib, W.; Müller-Buschbaum, H. Ein Neues Oxohalogenoferrat: $Sr_3Fe_2O_5Cl_2$. *Z. Anorg. Allg. Chem.* **1984**, *518*, 115−119.

(15) Gunnar Sillén, L.; Jörnstad, E. Einige Gemischte Wismutoxyjodide. *Z. Anorg. Allg. Chem.* **1942**, *250*, 173−198.

(16) Gutau, W.; Müller-Buschbaum, H. Über Ein Neues Halogenooxoindat: $Ba_3In_2O_5Cl_2$ Mit $Sr_3Ti_2O_7$-Struktur. *Z. Anorg. Allg. Chem.* **1990**, *584*, 125−128.

(17) Letouzé, F.; Martin, C.; Pelloquin, D.; Michel, C.; Hervieu, M.; Raveau, B. A Thallium Oxychloride Closely Related to the $Sr_3Ti_2O_7$ and $YBaFeCuO_5$ Structures: $Ba_3Tl_2O_5Cl_2$. *Mater. Res. Bull.* **1996**, *31*, 773−780.

(18) *Rigaku Oxford Diffraction CrysAlisPro*, version 1.171.38.43; Rigaku Corp.: Oxford, U.K., 2016.

(19) Betteridge, P. W.; Carruthers, J. R.; Cooper, R. I.; Prout, K.; Watkin, D. J. *CRYSTALS* Version 12: Software for Guided Crystal Structure Analysis. *J. Appl. Crystallogr.* **2003**, *36*, 1487.

(20) Palatinus, L.; Chapuis, G. SUPERFLIP - a Computer Program for the Solution of Crystal Structures by Charge Flipping in Arbitrary Dimensions. *J. Appl. Crystallogr.* **2007**, *40*, 786−790.

(21) Groom, C. R.; Bruno, I. J.; Lightfoot, M. P.; Ward, S. C. The Cambridge Structural Database. *Acta Crystallogr., Sect. B: Struct. Sci., Cryst. Eng. Mater.* **2016**, *72*, 171−179.

(22) Singh, D. J.; Nordstrom, L. *Planewaves, Pseudopotentials and the LAPW Method*, 2nd ed.; Springer: Berlin, 2006.

(23) Schwarz, K.; Blaha, P.; Madsen, G. Electronic Structure Calculations of Solids Using the WIEN2k Package for Material Sciences. *Comput. Phys. Commun.* **2002**, *147*, 71−76.

(24) Perdew, J. P.; Burke, K.; Ernzerhof, M. Generalized Gradient Approximation Made Simple. *Phys. Rev. Lett.* **1996**, *77*, 3865−3868.

(25) Whalen, J. B.; Besara, T.; Vasquez, R.; Herrera, F.; Sun, J.; Ramirez, D.; Stillwell, R. L.; Tozer, S. W.; Tokumoto, T. D.; McGill, S. A.; Allen, J.; Davidson, M.; Siegrist, T. A New Oxytelluride: Perovskite and CsCl Intergrowth in $Ba_3Yb_2O_5Te$. *J. Solid State Chem.* **2013**, *203*, 204−211.

(26) Iandelli, A.; Palenzona, A. Atomic Size of Rare Earths in Intermetallic Compounds. MX Compounds of CsCl Type. *J. Less-Common Met.* **1965**, *9*, 1−6.

DOI: 10.1021/acs.inorgchem.7b02265
Inorg. Chem. 2018, 57, 1727−1734

(27) Besara, T.; Lundberg, M. S.; Sun, J.; Ramirez, D.; Dong, L.; Whalen, J. B.; Vasquez, R.; Herrera, F.; Allen, J. R.; Davidson, M. W.; Siegrist, T. Single Crystal Synthesis and Magnetism of the BaLn_2O_4 Family (Ln = Lanthanide). *Prog. Solid State Chem.* **2014**, *42*, 23−36.
(28) Brese, N. E.; O'Keeffe, M. Bond-Valence Parameters for Solids. *Acta Crystallogr., Sect. B: Struct. Sci.* **1991**, *47*, 192−197.
(29) Gagné, O. C.; Hawthorne, F. C. Comprehensive Derivation of Bond-Valence Parameters for Ion Pairs Involving Oxygen. *Acta Crystallogr., Sect. B: Struct. Sci., Cryst. Eng. Mater.* **2015**, *71*, 562−578.
(30) Ramirez, A. P. Strongly Geometrically Frustrated Magnets. *Annu. Rev. Mater. Sci.* **1994**, *24*, 453−480.
(31) Knee, C. S.; Field, M. A. L.; Weller, M. T. Neutron Diffraction Study of the Antiferromagnetic Oxyhalides $Sr_3Fe_2O_5Cl_2$, $Sr_3Co_2O_5Cl_2$ and $Sr_3FeCoO_5Cl_2$. *Solid State Sci.* **2004**, *6*, 113−450.
(32) Wollan, E. O.; Koehler, W. C. Neutron Diffraction Study of the Magnetic Properties of the Series of Perovskite-Type Compounds [(1-x)La, xCa]MnO_3. *Phys. Rev.* **1955**, *100*, 545−563.
(33) Mironov, V. S. Superexchange Interaction between Lanthanide f^1 Ions. Spin-Hamiltonian Calculations for the 90° and 180° f^1-f^1 Superexchange. *J. Phys.: Condens. Matter* **1996**, *8*, 10551−10580.

DOI: 10.1021/acs.inorgchem.7b02265
Inorg. Chem. 2018, 57, 1727−1734